PHYSICAL REVIEW B **86**, 155121 (2012)

# Approaching finite-temperature phase diagrams of strongly correlated materials: A case study for $V_2O_3$

Daniel Grieger, Christoph Piefke, Oleg E. Peil, and Frank Lechermann
*I. Institut für Theoretische Physik, Universität Hamburg, Jungiusstr. 9, D-20355 Hamburg, Germany*
(Received 23 July 2012; published 10 October 2012)

Examining phase stabilities and phase equilibria in strongly correlated materials asks for a next level in the many-body extensions to the local-density approximation (LDA) beyond mainly spectroscopic assessments. Here, we put the charge-self-consistent LDA + dynamical mean-field theory (DMFT) methodology based on projected local orbitals for the LDA + DMFT interface and a tailored pseudopotential framework into action in order to address such thermodynamics of realistic strongly correlated systems. Namely, a case study for the electronic phase diagram of the well-known prototype Mott-phenomena system $V_2O_3$ at higher temperatures is presented. We are able to describe the first-order metal-to-insulator transitions with negative pressure and temperature from the self-consistent computation of the correlated total energy in line with experimental findings.

DOI: 10.1103/PhysRevB.86.155121 PACS number(s): 71.45.Gm, 71.45.Lr, 71.30.+h, 73.20.Mf

## I. INTRODUCTION

The first-principles computation of phase diagrams at finite temperature $T$ for multicomponent materials systems is a quite formidable challenge. Although there are very successful (semi)empirical methodologies to compute the thermodynamics of binary (or higher) realistic systems, most notably the CALPHAD approach,[1] the capability of predicting phase diagrams by starting from an *ab initio* quantum mechanical level has a rather strong appeal to many theorists. Dating back to the pioneering work in this research area by Hume-Rothery in the 1930s through empirical rules based on atomic sizes and electronegativities,[2,3] the field has reached quite a level of sophistication. After the extension of Hume-Rothery's original ideas by Miedema and co-workers[4] via additionally introducing the electronic charge density in the determination of the formation energy, approaches built on density functional theory (DFT) in the Kohn-Sham representation[5] eventually have taken over and have been dominating the research on atomistic phase-diagram calculations[6–9] since the mid 1980s (see, e.g., Ref. 10 for a review).

However, materials systems with less-screened Coulomb interactions among the electrons of the order of, or larger than, the bandwidth $W$ have remained so far out of reach. Conventional representations of DFT, via, e.g., the local-density approximation (LDA),[5] are not capable of accounting for the effects of strong electronic correlations. Phase transformations at finite $T$ either of pure electronic kind or driven by electronic correlations are usually not describable solely within Bloch band theory. On the other hand, many novel materials, which are technologically promising because of, e.g., enhanced response behavior, display signatures of strong correlations. Furthermore, even well-known allotropes of transition metals or prominent transition-metal alloys with or close to magnetic order (such as, e.g., the iron-aluminum system)[11] are rather difficult to model within standard LDA(-like) approaches due to the lack of explicit many-body correlation effects.

The combination of LDA with the dynamical mean-field theory (DMFT), the so-called LDA + DMFT approach, nowadays prosperously allows us to include the effects of strong Coulomb interactions in realistic solids (see, e.g., Ref. 12 for a review). Note that one may easily use the generalized-gradient approximation (GGA) for the DFT part, but as far as it concerns explicit strong correlation effects, the difference to the LDA approach is usually negligible. Yet, there are only few implementations that handle the LDA + DMFT formalism in a charge self-consistent framework, i.e., accounting for the feedback of the local electronic self-energy onto the charge density that determines the Kohn-Sham effective potential, until self-consistency of the complete interacting charge density is achieved.[12–18] Additionally, in order to account for competing strongly correlated phases at elevated temperatures, there are high demands on the accuracy and generality of the underlying band-structure methodology as well as the utilized DMFT impurity solver.

As to explicit realistic phase-competition studies, there is prominent work within that scope mainly in the area of $f$-electron compounds.[12,21] In a recent LDA + DMFT study, Leonov *et al*. provided a quite successful modeling of the high-temperature bcc-to-fcc transition in iron[22] using the powerful quantum Monte Carlo method for the impurity solution. However, there the charge self-consistency was neglected and total energies have been calculated in a post-processing scheme.

In this work, we want to review the current state of the art formalism for handling the charge-self-consistent LDA + DMFT method with the direct calculation of the correlated total energy. The full approach is applied to the key features of the electronic phase diagram of the famous sesquioxide $V_2O_3$ (see Fig. 1) above room temperature. When revealing the phase boundaries between metallic and insulating phases with $T$ and pressure $p$, we neglect the effect of chemical disorder as well as explicit electronic entropy contributions. The former is not expected to play a vital role in this study since we are interested in the stoichiometric system well below possible disordering/melting temperatures. Extending the strongly correlated formalism to composition-dependent phase diagrams is in principle possible, e.g., via the so-called stat-DMFT method.[23] As it will be shown, the present results in the more restricted scheme are already encouraging, and it should be mainly a matter of time when such new and further elaborate techniques will become a generic tool in the context of first-principles phase-diagram evaluations.

 

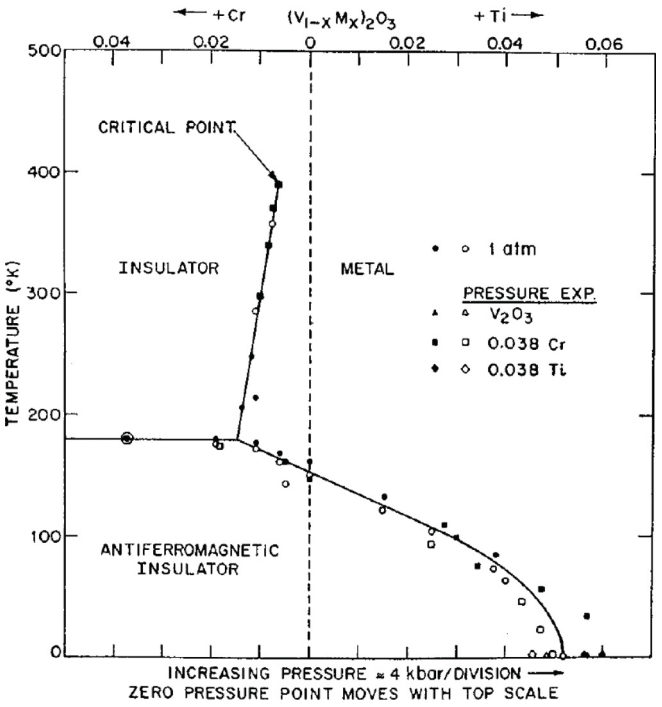


FIG. 1. Experimental phase diagram of $V_2O_3$ from Refs. 19 and 20.

## II. THEORETICAL FRAMEWORK

The charge-self-consistent scheme of the LDA + DMFT framework is technically and computationally rather demanding and only few implementations thereof exist up to now.[14–18] For the DFT(LDA) part of the calculations, we here employ a mixed-basis pseudopotential[24] (MBPP) as well as a projector-augmented wave[25] (PAW) implementation.

The explicit many-body effects are treated within a multiorbital Hubbard model including also all non-density-density local interaction terms. We choose to parametrize the resulting complete Coulomb matrix with two interaction integrals, namely, the Hubbard $U$ and the Hund's exchange $J$. Thus, we neglect differentiations in these matrix elements originating from the nonspherical symmetry due to the crystal environment. The interacting problem is solved within DMFT using a continuous-time quantum Monte Carlo (CT-QMC) impurity solver in the hybridization-expansion formulation[26] as implemented in the TRIQS package.[27]

In short, the charge-self-consistency condition can on equal footing be understood as a way of improving the density functional of DFT to include more explicit correlation effects as well as finding a realistic and consistent effective single-particle part of DMFT via combining both formalisms to a new, complete cycle, which is summarized in the following sections.

Before that, however, it is vital to note that on general grounds, this LDA + DMFT formalism is manifestly temperature dependent and therefore in principle ideally suited for thermodynamic problems. This is in stark contrast to the standard extension of the Kohn-Sham formalism towards finite $T$ via the Mermin theory of including the proper Fermi function for the electronic states.[28] Here, the full impact of temperature on the many-body level, including, e.g., the effective disappearance of Bloch-type quasiparticle states and thus the localization due to the loss of coherency at large $T$, is properly taken care of.

### A. Projected local orbitals

The DFT(LDA) method utilizes an orbital-independent representation of the effective-single-particle Hamiltonian for the electronic structure resulting in Bloch Kohn-Sham (KS) wave functions for the solid-state electronic structure. On the other hand, the DMFT equations make use of a local correlated subspace in order to include the effects of strong Coulomb correlations in condensed matter. Thus, the first step that has to be performed when interfacing the DFT(LDA) and the DMFT technique is the extraction of a suitable correlated subspace $\mathcal{C}$ starting from the complete Hilbert space of Bloch KS band states. This is done in the projected-local-orbitals (PLO) scheme.[29–32] For completeness, we here briefly review the methodology in the context of charge self-consistency and the total-energy calculation. More details may be found in Ref. 31.

Normalized orthogonal projections onto chosen local orbitals with character $m$ and centered at site $\underline{R}$ may be defined via

$$\tilde{P}^{\underline{R}}_{m\nu}(\underline{k}) \equiv \sum_{\underline{R}'m'} \{[\underline{\underline{O}}(\underline{k})]^{-\frac{1}{2}}\}^{\underline{R}\underline{R}'}_{mm'} \langle \chi_{\underline{R}m'} | \Psi_{\underline{k}\nu} \rangle, \tag{1}$$

where the $|\Psi_{\underline{k}\nu}\rangle$ for wave vector $\underline{k}$ and band $\nu$ are chosen to be a subset $\mathcal{W}$ of the Bloch states of the original LDA treatment and $\underline{\underline{O}}$ describes the overlap matrix written as

$$O^{\underline{R}\underline{R}'}_{mm'}(\underline{k}) \equiv \sum_{\nu \in \mathcal{W}} \langle \chi_{\underline{R}m} | \Psi_{\underline{k}\nu} \rangle \langle \Psi_{\underline{k}\nu} | \chi_{\underline{R}'m'} \rangle. \tag{2}$$

The set of states $\{|\chi_{\underline{R}m}\rangle\}$ together with the energy window $\mathcal{W}$ define the correlated subspace $\mathcal{C}$, chosen such that the problem of strong local Coulomb interactions is adequately represented. Conveniently, $\mathcal{C}$ is adapted to an available localized basis used in a given band-structure code, i.e., linear combinations of the mixed basis within the MBPP framework or the partial waves of PAW.

Using the projections (1), one can construct the one-particle Green's function within the truncated Bloch space $\mathcal{W}$ via the double-counting corrected local DMFT self-energy [written in Matsubara frequencies $\omega_n = (2n+1)\pi k_B T$], which is assumed block diagonal in the correlated sites, written as

$$\Delta\underline{\underline{\Sigma}}^{\underline{R}\underline{R}'}(i\omega_n) \equiv (\underline{\underline{\Sigma}}^{\mathrm{imp},\underline{R}}(i\omega_n) - \underline{\underline{\Sigma}}^{\mathrm{dc},\underline{R}})\delta_{\underline{R}\underline{R}'}. \tag{3}$$

This Bloch Green's function is thereby connected to the correlated subspace through an upfolding procedure, i.e.,

$$\underline{\underline{G}}^{\mathrm{bl}}(i\omega_n,\underline{k}) = \Bigg[ (i\omega_n + \mu)\underline{\underline{1}} - \underline{\underline{\epsilon}}^{\mathrm{KS}}_{\underline{k}} - \sum_{\underline{R}\underline{R}'} \underline{\underline{\tilde{P}}}^{\underline{R}\dagger}(\underline{k}) \cdot \Delta\underline{\underline{\Sigma}}^{\underline{R}\underline{R}'}(i\omega_n) \cdot \underline{\underline{\tilde{P}}}^{\underline{R}'}(\underline{k}) \Bigg]^{-1}. \tag{4}$$

In this equation, $\underline{\underline{\epsilon}}^{\mathrm{KS}}_{\underline{k}}$ denotes the diagonal matrix of Kohn-Sham eigenvalues for the Bloch states and $\mu$ marks the chemical potential (see Sec. II D for details). This Green's function

can then be downfolded to the correlated subspace, enforcing the DMFT self-consistency condition (proper normalization of the $k$ sum here and in the following is understood)

$$\underline{\underline{G}}^{\mathrm{imp},\underline{R}}(i\omega_n) \equiv \sum_{\underline{k}} \underline{\underline{\bar{P}}}^{\underline{R}}(\underline{k}) \cdot \underline{\underline{G}}^{\mathrm{bl}}(i\omega_n,\underline{k}) \cdot \underline{\underline{\bar{P}}}^{\underline{R}\dagger}(\underline{k}). \tag{5}$$

This impurity Green's function can then be used to supply a new DMFT bath Green's function

$$(\underline{\underline{\mathcal{G}_0}}^{\underline{R}})^{-1}(i\omega_n) = (\underline{\underline{G}}^{\mathrm{imp},\underline{R}})^{-1}(i\omega_n) + \underline{\underline{\Sigma}}^{\mathrm{imp},\underline{R}}(i\omega_n) \tag{6}$$

that enters the impurity solver yielding eventually an updated impurity self-energy until convergence is achieved. The outlined iterative scheme marks the usual DMFT cycle without charge self-consistency since it then works as post-processing scheme to a once computed set of Kohn-Sham objects $\{\epsilon^{\mathrm{KS}}_{\underline{k}\nu}, \Psi_{\underline{k}\nu}\}$.

### B. Expressing charge densities

The fundamental step in the *self-consistent* combination of DFT(LDA) and DMFT is provided by the expression of the basic quantities of each method in terms of the basic quantities of the other method. Namely, charge density for DFT and one-particle Green's function for DMFT. For this purpose, we define a Kohn-Sham Green's function through

$$\underline{\underline{G}}^{\mathrm{KS}}(i\omega_n,\underline{k}) = \left[(i\omega_n + \mu_{\mathrm{KS}})\underline{\underline{1}} - \underline{\underline{\epsilon}}^{\mathrm{KS}}_{\underline{k}}\right]^{-1}. \tag{7}$$

Note that this function is in general different from the DMFT "Weiss-Field" $\mathcal{G}_0$. The choice of $\mu_{\mathrm{KS}}$ is described in detail in Sec. II D. In the following, the band indices $\nu\nu'$ live in the truncated Bloch Hilbert space $\mathcal{W}$ and we drop for convenience the site index $\underline{R}$. Generalization of the formulas including the latter is straightforward and since the charge density is additive, contributions from (supposedly weakly correlated) bands outside $\mathcal{W}$ are most easily taken care of. The trace of $\underline{\underline{G}}^{\mathrm{KS}}(i\omega_n,\underline{k})$ expressed in the Bloch basis is nothing else than the charge density of a stand-alone KS-LDA calculation which reads as

$$\rho^{\mathrm{KS}}(\underline{r}) = \frac{1}{\beta} \sum_{\underline{k}n\nu\nu'} \langle \underline{r}|\Psi_{\underline{k}\nu}\rangle\, G^{\mathrm{KS}}_{\nu\nu'}(i\omega_n,\underline{k})\, \langle \Psi_{\underline{k}\nu'}|\underline{r}\rangle, \tag{8}$$

with $\beta = 1/k_{\mathrm{B}}T$ as the inverse temperature. A very similar form can be found for the charge density from a post-processing DMFT calculation, i.e.,

$$\rho(\underline{r}) = \frac{1}{\beta} \sum_{\underline{k}n\nu\nu'} \langle \underline{r}|\Psi_{\underline{k}\nu}\rangle\, G^{\mathrm{bl}}_{\nu\nu'}(i\omega_n,\underline{k})\, \langle \Psi_{\underline{k}\nu'}|\underline{r}\rangle. \tag{9}$$

Thus, the difference $\rho'(\underline{r}) = \rho(\underline{r}) - \rho^{\mathrm{KS}}(\underline{r})$ is given by

$$\begin{aligned}\rho'(\underline{r}) = \frac{1}{\beta} \sum_{\underline{k}n\nu\nu'} \langle \underline{r}|\Psi_{\underline{k}\nu}\rangle \{&\underline{\underline{G}}^{\mathrm{KS}}(i\omega_n,\underline{k}) \cdot ((\underline{\underline{G}}^{\mathrm{KS}})^{-1}(i\omega_n,\underline{k}) \\ &- (\underline{\underline{G}}^{\mathrm{bl}})^{-1}(i\omega_n,\underline{k})) \cdot \underline{\underline{G}}^{\mathrm{bl}}(i\omega_n,\underline{k})\}_{\nu\nu'} \langle \Psi_{\underline{k}\nu'}|\underline{r}\rangle \\ \equiv \sum_{\underline{k}\nu\nu'} &\langle \underline{r}|\Psi_{\underline{k}\nu}\rangle\, \Delta N_{\nu\nu'}(\underline{k})\, \langle \Psi_{\underline{k}\nu'}|\underline{r}\rangle.\end{aligned} \tag{10}$$

As described in Ref. 33, the object $\underline{\underline{\Delta N}}(\underline{k})$ can be rewritten as

$$\begin{aligned}\underline{\underline{\Delta N}}(\underline{k}) = \frac{1}{\beta} \sum_{n} \{&\underline{\underline{G}}^{\mathrm{KS}}(i\omega_n,\underline{k}) \cdot (\underline{\underline{\bar{P}}}^{\dagger}(\underline{k}) \cdot \Delta\underline{\underline{\Sigma}}(i\omega_n) \cdot \underline{\underline{\bar{P}}}(\underline{k}) \\ &- (\mu - \mu_{\mathrm{KS}})\underline{\underline{1}}) \cdot \underline{\underline{G}}^{\mathrm{bl}}(i\omega_n,\underline{k})\}.\end{aligned} \tag{11}$$

Therewith a simple representation of the total charge density including self-energy effects beyond LDA is provided, reading as

$$\rho(\underline{r}) = \sum_{\underline{k}\nu\nu'} \langle \underline{r}|\Psi_{\underline{k}\nu}\rangle (f(\tilde{\epsilon}_{\underline{k}\nu})\delta_{\nu\nu'} + \Delta N_{\nu\nu'}(\underline{k}))\langle \Psi_{\underline{k}\nu'}|\underline{r}\rangle \tag{12}$$

and to be used and manipulated in a given DFT-based band-structure code. Here, $f(\epsilon)$ denotes the Fermi-distribution function and $\tilde{\epsilon}_{\underline{k}\nu} = \epsilon_{\underline{k}\nu} - \mu_{\mathrm{KS}}$. Hence, the inclusion of the DMFT self-energy renders it necessary to not only incorporate modifying terms diagonal in the Bloch states, but also off-diagonal contributions. The problem of truncating the whole Bloch space to a subspace $\mathcal{W}$ therefore reduces to taking into account the correct set of bands in each summand. Details on the implementation thereof in the different KS basis sets are given in the Appendix.

### C. Self-consistency condition

The aim of charge self-consistency is to include DMFT self-energy effects in the charge density, so that $\rho^{\mathrm{KS}}(\underline{r})$ and $\rho(\underline{r})$ can obviously not be the same quantity. Instead, it is most instructive to use the (spectral density-) functional approach by Savrasov and Kotliar,[34] incorporating both one-particle Green's functions and charge density. Extremization thereof with respect to the charge density $\rho(\underline{r})$ basically yields the Kohn-Sham equations in which the correlated charge density $\rho(\underline{r})$ is used as an input for the effective potential $\hat{V}_{\mathrm{eff}}[\rho(\underline{r})]$, i.e.,

$$[\hat{T} + \hat{V}_{\mathrm{eff}}[\rho(\underline{r})] - \epsilon_{\underline{k}\nu}]|\Psi_{\underline{k}\nu}\rangle = 0. \tag{13}$$

Similarly, extremization with respect to the Green's function yields the usual expression for the DMFT self-energy. Thus, the complete cycle can be constructed as follows: From an initial DFT(LDA) calculation, perform conventional DMFT steps and compute a correlated charge density $\rho(\underline{r})$ as given by Eq. (12). That charge density is reinserted into the band-structure code [for this step, knowing the elements of $\underline{\underline{\Delta N}}(\underline{k})$ is sufficient] and new effective-single-particle wave functions $|\Psi_{\underline{k}\nu}\rangle$ are computed using Eq. (13). These finally enter Eq. (1) to build a new correlated subspace for DMFT (keeping the set $\{|\chi_{\underline{R}m}\rangle\}$ unaltered). This enlarged cycle is iterated until full charge self-consistency is reached, i.e., charge density and self-energies (and thus the matrix $\underline{\underline{\Delta N}}^{(\underline{k})}$) remain constant with iterations. From our experience, the cycle is usually rapidly converging when using already a rather simple linear-mixing scheme.

### D. Chemical potential

As usual, the chemical potential $\mu$ is adjusted such that the resulting total charge density $\rho_{\mathrm{tot}}(\underline{r})$ holds the correct total

number of electrons $N_{\rm tot}$ and is enforced via

$$\int d\underline{r}\ \rho_{\rm tot}(\underline{r}) = N_{\nu\notin\mathcal{W}} + \frac{1}{\beta}\sum_{\underline{k}n\nu} G^{\rm bl}_{\nu\nu}(i\omega_n,\underline{k}) = N_{\rm tot}. \qquad (14)$$

In Ref. 33, it is argued that this charge neutrality condition is imposed on $\rho_{\rm tot}(\underline{r})$ only [not on $\rho^{\rm KS}(\underline{r})$]. Thus, the parameter $\mu_{\rm KS}$, which is defined to be the energy up to which the Kohn-Sham states of the DFT(LDA) part are filled (with the proper Fermi-distribution function), can be chosen to be equal to the chemical potential $\mu$, which would mean that the integrated charge density changes due to correlations in Eq. (12) vanishes.

However, in order to clarify relations between some of the quantities that occur in the formalism, it can be useful to choose $\mu_{\rm KS}$ such that the DFT(LDA) part of the calculation is already charge neutral. It can easily be shown that with the correction term of Eq. (11), this choice does not affect $\rho(\underline{r})$. Anyway, it is important to note that $\mu_{\rm KS}$ itself has no physical interpretation in the enlarged LDA + DMFT framework.

### E. Total energy

In order to obtain total energies within the charge-self-consistent formalism, the spectral density-functional approach is applied again. Based thereon, the total energy may be computed from[14]

$$E_{\rm LDA+DMFT} = E_{\rm LDA} + \sum_{\underline{k}\nu} \epsilon^{\rm KS}_{\underline{k}\nu}\,\Delta N^{(\underline{k})}_{\nu\nu} + \langle \hat{H}_U\rangle - E_{\rm dc}. \qquad (15)$$

Note that this expression relies on the fact that the adapted diagonal basis for the Kohn-Sham single-particle Hamiltonian is utilized, which yields eigenvalues $\epsilon^{\rm KS}_{\underline{k}\nu}$. Several approaches are possible to obtain the expectation value of the two-particle Hamiltonian $\langle \hat{H}_U\rangle$. Here, we choose to apply the Galitskii-Migdal formula.[35] As shown by Boehnke *et al.*,[36] the quality of the numerical data can be improved by choosing a suitable basis set, i.e., Legendre polynomials, for the representation of the one-particle Green's function. Note that although this LDA + DMFT total energy is temperature dependent, we here keep the "energy" notion since for a well-defined "free energy," a clear definition of an entropic part would be in order.

## III. $V_2O_3$ SYSTEM

The vanadium sesquioxide $V_2O_3$ belongs to the most prominent strongly correlated compounds and has already been subject to many theoretical efforts.[37–44] At elevated temperatures, it orders in the corundum structure in which there are V-V pairs along the crystallographic $c$ axis and a honeycomb lattice appears in the $xy$ plane (see Fig. 2). The V ions reside within an octahedron of oxygen ions, respectively, building up a trigonal crystal field for the transition-metal ion. Thus, the low-energy $t_{2g}$ orbitals of the V($3d$) shell are split into an $a_{1g}$ and two degenerate $e'_g$ orbitals. Formally, the vanadium ion has the $3d^2$ valence configuration, i.e., is in the $V^{3+}$ oxidation state. The $t_{2g}$ orbital degrees of freedom appear to play a central role for the intriguing physics of this transition-metal oxide, and Castellani *et al.*[37] were the first to provide a detailed account of the complex correlated electronic structure in these local terms.

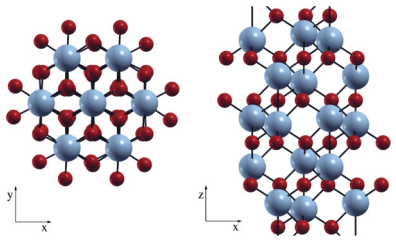


FIG. 2. (Color online) Corundum structure of $V_2O_3$ viewed along the $z$ axis (left) and along the $y$ axis (right), with depicted V ions (large gray) and O ions (small red/dark).

The finite-temperature phase diagram, taken from the original work of McWhan and co-workers,[19,20] is shown in Fig. 1. In this work, V substitution by Ti (Cr) implies positive (negative) pressure. It displays three major phases, namely, paramagnetic metallic (PMM), paramagnetic insulating (PMI), as well as an antiferromagnetic insulating (AFI) regime. The transition to the latter AFI phase at lower temperatures is also associated with a structural transition to a monoclinic low-symmetry structure.[39] Furthermore, additional phase-diagram studies in the vanadium-deficient $V_{2-y}O_3$ regime revealed the existence of a metallic spin-density-wave (SDW) phase.[45] Interestingly, that phase appears not to be a form of precursor to the much more extended AFM ordering of the insulator. On the contrary, it seems that the magnetic short-range order within PMM and PMI is closer to the SDW ordering. Therefore, the magnetic ordering in the AFI phase may be closely related to the structural change, even involving additional orbital ordering.[46] Due to this additional complexity in connection with the AFI phase, we concentrate in this work only on the phase equilibrium between PMM and PMI. A complete description of the $V_2O_3$ phase diagram including the magnetically ordered phases will be postponed to future studies.

### A. LDA characterization and local projections

A thorough first-principles DFT(LDA) description of metallic $V_2O_3$ at normal pressure and without doping has initially been given by Mattheiss.[38] Here, we only summarize the most relevant features as they evolve from our MBPP investigation. Figure 3 shows the LDA band structure along high-symmetry lines within the first Brillouin zone. It is evident that the bands group in a way canonical for many

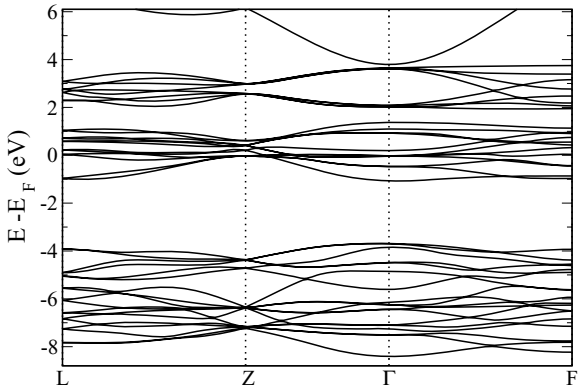


FIG. 3. LDA band structure of $V_2O_3$.

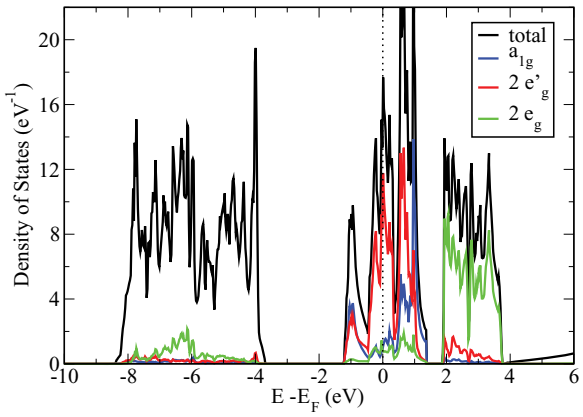


FIG. 4. (Color online) Total LDA density of states of $V_2O_3$ and local DOS within the symmetry-adapted V($3d$) basis with range $r_c = 2.0$ a.u.

transition-metal oxides. The larger block below the Fermi level $\epsilon_F$ in the range $[-8, -4]$ eV is dominated by oxygen $2p$ orbital weight, while the unoccupied block within [2,4] eV stems primarily from vanadium $e_g$ orbitals. This encoding is visualized in the density-of-states (DOS) plot of Fig. 4 from local projections onto the symmetry-adapted cubic-harmonic angular-momentum channel of the V($3d$) basis. The band manifold of width $W \sim 2.6$ eV around $\epsilon_F$ is mostly composed of $a_{1g}$ and $e'_g$ orbitals with only minor inter-mixing of V($e_g$) and O($2p$). Note that especially the $a_{1g}$ character shows a prominent bonding-antibonding signature in the DOS of this low-energy region.

From the LDA result, the set of local orbitals $\{|\chi_{\underline{R}m}\rangle\}$ to be utilized in the local projections defined in Eq. (1) are here chosen to be given by the linear combinations of pseudized atomic $V(3d)$ functions that diagonalize the orbital density matrix on each of the four symmetry-equivalent vanadium ions within the unit cell. This is often referred to as the crystal-field basis, whereby here the $a_{1g}$ level is higher in energy than the $e'_g$ one. Figure 5 exhibits the local DOS obtained from the projections using for $\mathcal{W}$ the low-energy $t_{2g}$ manifold. In the following, we will only concentrate on these minimal projected local orbitals and will not elaborate on the possible cases of

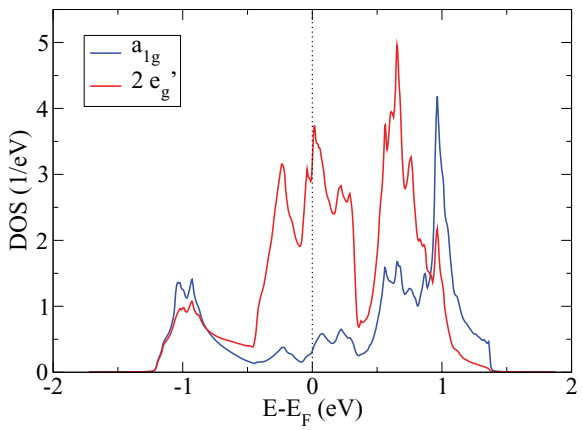


FIG. 5. (Color online) $a_{1g}$ and $e'_g$ LDA-DOS on the basis of the orthonormalized projected local orbitals, whereby the range of the $\{|\chi_{\underline{R}m}\rangle\}$ was also $r_c = 2.0$ a.u.

larger energy windows $\mathcal{W}$, i.e., such ones that also cover the high-energy occupied/unoccupied band manifolds. Note that the local orbital DOS in Figs. 4 and 5 differ on principle grounds (see also Sec. III). In the latter case, it is computed in the basis of orthonormalized orbitals, whereas in the former case it is calculated from projections onto angular-momentum channels without proper final normalization (i.e., no radial orbital function involved). From the orthonormalized projected local orbitals, one retrieves the occupations $n_{\mathrm{LDA}}(a_{1g}) = 0.57$ and $n_{\mathrm{LDA}}(e'_g) = 1.43$ (summed over both $e'_g$ orbitals), respectively. These values differ by about 0.05 electrons towards stronger orbital polarization compared to the numbers presented in Ref. 44 from a Wannier construction within the $N$th-order muffin-tin-orbital method.[47]

The stronger ionic character of the transition-metal oxide compared to ordinary metals or intermetallic compounds becomes clear from the plot of the bonding charge densities in Fig. 6. The latter function is defined as the difference between the crystal valence charge density and the superposed atomic valence charge densities. The charge transfer from vanadium to oxygen is obvious, but also the expected charge accumulation in the interstitial region is visible.

### B. LDA + DMFT: Finite-temperature phase equilibria

The LDA-only description does not account for a metal-insulator transition (MIT) in $V_2O_3$. We model the interacting problem on the many-body level within a three-orbital ($a_{1g}$, $2e'_g$) multisite (four V ions in the corundum unit cell) generalized Hubbard model employing the complete rotational invariant Coulomb interactions on the local level. For the parametrization of the Coulomb integrals, we choose the values $U = 5$ eV and $J = 0.93$ eV, as already utilized in earlier simplified LDA + DMFT studies for $V_2O_3$.[42] The following results are obtained from our MBPP-code interface of LDA + DMFT. A second implementation within the PAW approach is also briefly discussed in the Appendix.

#### 1. *Lattice expansion and temperature variation for fixed c/a ratio*

The MIT between the PMM and the PMI phase with negative pressure is depicted in Fig. 7 for selected $T$. While the $p < 0$ scenario is realized experimentally via Cr doping, it is here provided in a simple way by increasing the lattice constant $a$ starting from its experimental[48] equilibrium value $a_0 = 4.95$ Å. Notably, we also first keep the $c/a$ ratio fixed to its value $c/a = 2.83$ at ambient pressure and temperature. The effect of relaxing that ratio will be discussed in Sec. III B3. For the moment, this approximate theoretical approach proves to be sufficient to describe the key features of the $V_2O_3$ phase diagram above room temperature.

One could connect this approach to the physical pressure $p$ in a simple way by defining $p = -\partial E/\partial V$. It is seen that the theoretical formalism reveals the pressure-induced first-order MIT with the correct positive sign of the slope $\partial T_{\mathrm{MIT}}/\partial p$ from experiment (compare Fig. 1). However, the changes that occur in the lattice constant with $T$ along the phase boundary are nonsurprisingly larger (roughly by a factor 5–10) than in experiment.[49] The neglect of electronic and phononic entropy contributions (and presumably also nonlocal correlations) may be blamed. Nevertheless, the change of curvature of the

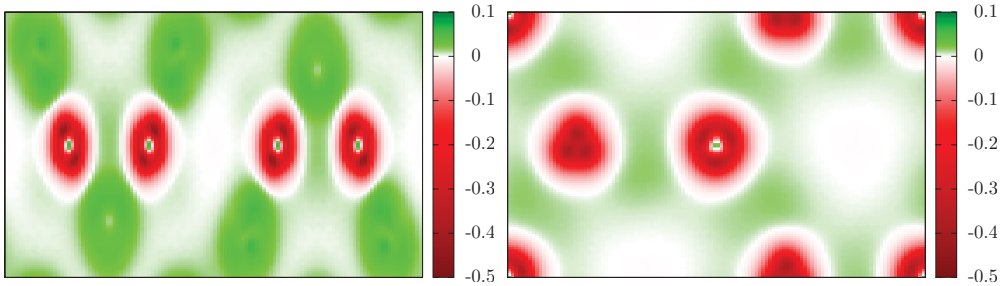


FIG. 6. (Color online) LDA bond charge densities $\rho^{\text{crystal}}(\underline{r}) - \rho^{\text{atomic}}(\underline{r})$ for $V_2O_3$ within the $xz$ plane (left) and the $xy$ plane (right). Note that in the latter case, the two central V ions are not at the same height and therefore appear different.

respective total energies elucidates the expected softening of the lattice with increasing temperature from the decrease of the bulk modulus $B \sim \frac{\partial^2 E}{\partial V^2}$. Figure 8 displays the tie-line construction for the first-order transition between the metallic and insulating phases. The volume jump at the transition becomes obvious, albeit again the retrieved pressure from the slope of the common tangent is about an order of magnitude too high compared to experiment. However, note that the increased stability range of the PMI phase with volume at larger $T$ is a direct result of the calculations. For $T_{\text{crit}} \sim 400$ K, the line of first-order transitions at negative pressure exhibits a solid-solid critical end point and a continuous path from the metallic to the insulating regime opens. One may already recognize that the shifted quasiparticle peak at the lower gap edge in the spectral function of the insulator has vanished for $T = 387$ K, which may signal the immediate strongly incoherent regime close to the critical end point.

The pressure-dependent investigation describes moreover the increase of correlation strength when approaching the critical $p$ deep from the metallic regime. This is documented in Fig. 9 where we plot the local spectral function with increasing lattice constant. Strong transfer of spectral weight from the low-energy region to the high-energy Hubbard bands is observable and marks the evolution towards the MIT with negative pressure at constant interaction strength. Furthermore, a shifting of the dominant quasiparticle peak towards the Fermi level with increasing the lattice constant may be recognized. Of course, the growing lattice distances also weaken the metallic screening and therefore should lead on simple grounds to an effective increase of the mutual Coulomb interaction between the electrons. Such an effect is here at least in simplest terms describable by the charge-self-consistent reaction to the applied lattice expansion. Note, however, in this context that recent photoemission studies point to a rather constant $U$ value on the different sides of the phase boundaries.[50]

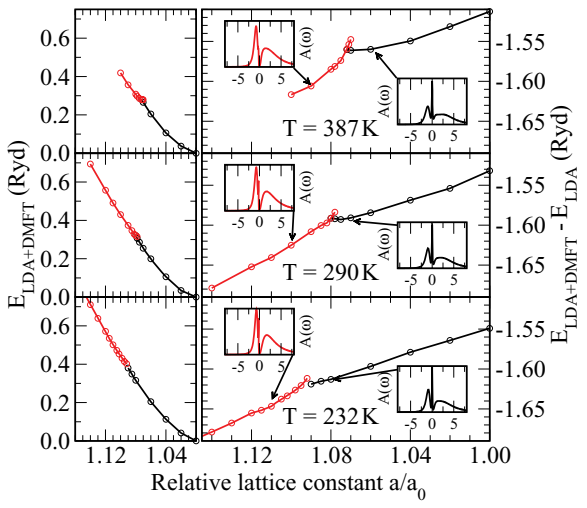


FIG. 7. (Color online) MIT with negative pressure, i.e., increase of the lattice constant for various temperatures within LDA + DMFT. Left: total energy $E_{\text{LDA+DMFT}}$ normalized to the value at the equilibrium lattice constant. Right: energies with respect to the LDA energy $E_{\text{LDA}}$ for each given lattice constant.

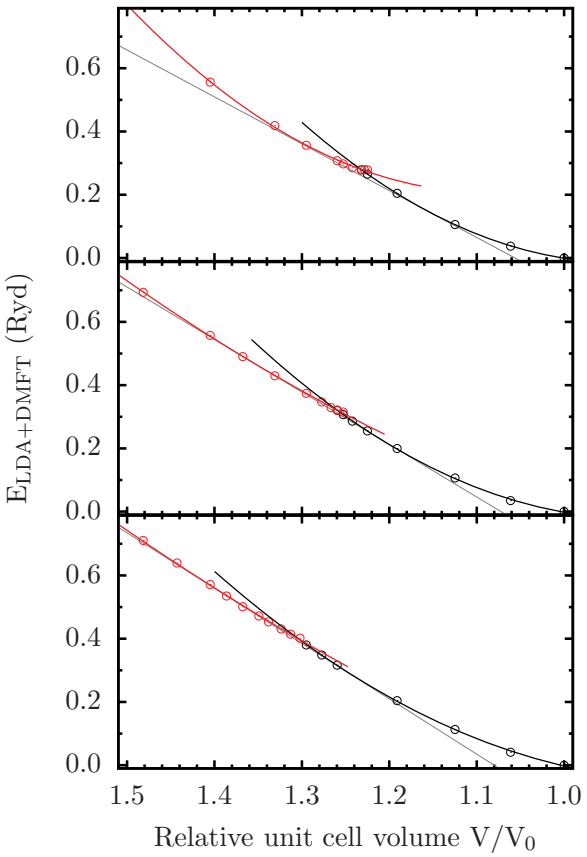


FIG. 8. (Color online) Tie-line construction for the first-order MIT with negative $p$ for $T = 387$, 290, and 232 K (from top to bottom).

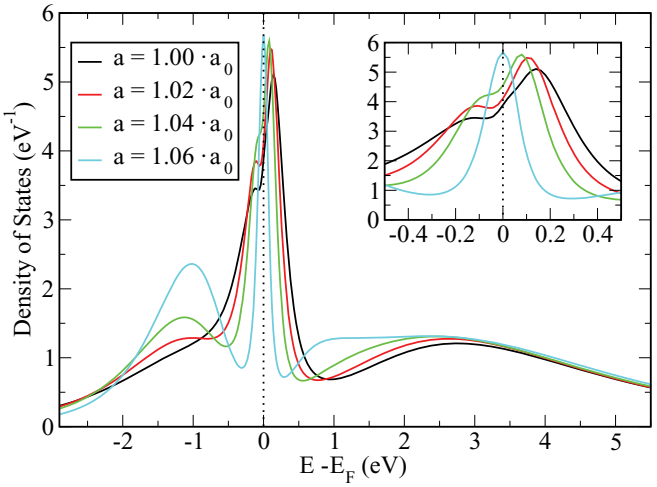


FIG. 9. (Color online) Evolution of the metallic spectral function with negative pressure for $T = 387$ K. The inset shows a blow-up of the features around the Fermi level.

In order to trace the MIT with temperature in some detail, we plot in Fig. 10 the intrinsically $T$-dependent LDA + DMFT energy now at fixed elongated lattice constant. Starting from the low-temperature metallic regime, $E_{\mathrm{LDA+DMFT}}(T)$ deviates from a simple functional behavior at $T \sim 270$ K, displaying an overall double-parabolic structure. The MIT takes place around $T_{\mathrm{MIT}} \sim 310$ K in good accordance with the expected experimental region of the temperature-induced PMM–PMI transition. Surprisingly, the energy $E_{\mathrm{LDA+DMFT}}(T)$ of the PMI phase appears rather flat in the temperature regime [350,450] K, which is just in the neighborhood of the experimental critical end point.

#### 2. *Charge densities and orbital resolution for fixed c/a ratio*

So far, we concentrated on the integral impact of the electronic correlation on the finite-temperature properties of the $V_2O_3$ system. However, for a deeper understanding of the underlying driving forces, it is also important to shed light on the possibly distinct behavior of individual microscopic degrees of freedom and most notably on those of orbital kind.

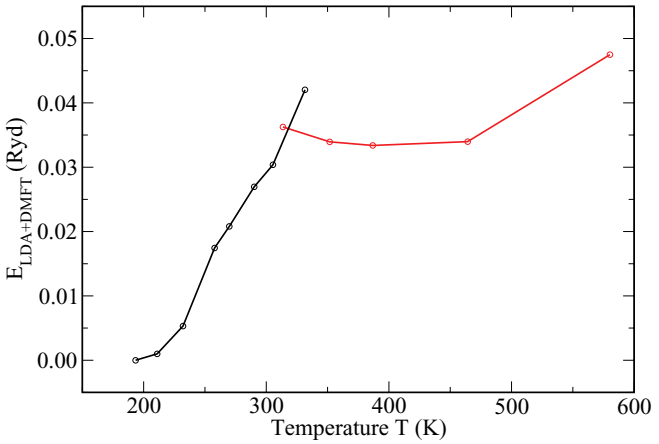


FIG. 10. (Color online) MIT with temperature for the fixed lattice constant $a = 1.08a_0$, i.e., at finite negative pressure.

Concerning the distinct orbital occupations with temperature and negative pressure, no dramatic effects occur in the correlated electronic structure. In line with previous post-processing studies,[43,44] within charge-self-consistent LDA + DMFT the $a_{1g}$ orbital filling is generally reduced compared to the LDA value (and correspondingly the $e'_g$ filling is increased). For the equilibrium volume and $T = 232$ K, the numbers write as $n_{\mathrm{DMFT}}(a_{1g}) = 0.48$ and $n_{\mathrm{DMFT}}(e'_g) = 1.52$. A real-space discrimination of these orbital filling differences between LDA + DMFT and LDA on the basis of the respective charge densities is displayed in Fig. 11 for $T$ close to the critical end point. In general, a localization effect takes place, whereby charge from the interstitial region is transferred closer to the atomic sites. Thereby, the $a_{1g}$ orbital (pointing roughly along the $z$ axis) loses charge in the correlated electronic structure, whereas the $e'_g$ orbitals gain.[43,44] In the insulating regime, less charge is transferred from the interstitial part, but note that here the lattice constant is also larger.

Within the correlated scheme, increasing the negative $p$, i.e., enhancing the lattice constant, yields a slight filling increase of the $a_{1g}$ orbital. When raising $T$ for $a = 1.08a_0$, so that the system shows a temperature-induced MIT, the same trend occurs. The same effect with temperature was already theoretically observed in Ref. 44. Thus, the calculation reveals an increase (decrease) in the occupation (of the order of a few percent) for the $a_{1g}$ ($e'_g$) orbital in the insulator compared to the metal. It is again instructive to visualize directly the changes in the self-consistent correlated charge density. Figure 12 depicts the differences in the LDA + DMFT charge density $\rho_{\mathrm{DMFT}}(\underline{r})$ at the different temperatures associated with the metallic and the insulating phases. It is seen that here the charge transfers are marginal, mainly showing the $a_{1g}$ orbitals gaining some charge against the $e'_g$ with $T$. As an effect of the temperature raise, the interstitial in-between the V ions appears to lose some small weight, in the spirit of effective localization at high $T$.

Finally, we turn to a brief look on the magnetic response. The orbital-resolved local spin susceptibility $\chi$, plotted in Fig. 13, shows for both orbital contributions the expected Curie-Weiss–type tail at higher temperatures, but for fixed lattice constant, a nonmonotonic behavior below $T \sim 270$ K emerges, i.e., in the same range where the nontrivial characteristic in $E_{\mathrm{LDA+DMFT}}(T)$ was observed. The quenching of $\chi_{a_{1g}}$ in that regime needs further study and might be interesting in the context of orbital ordering in the low-temperature AFI phase. As expected, for constant $T$ the increase of the lattice constant leads also to nearly constant $\chi$ in the PMI phase.

#### 3. *Effect of relaxing the c/a ratio*

From experiment it is known that the $c/a$ ratio is lowered when passing from the metal to the insulator with negative pressure.[49,51,52] In order to account for that effect, we relaxed $c/a$ for each volume $V$ within charge-self-consistent LDA + DMFT at $T = 387$ K by computing the total energy for selected $c/a$ values and finding the minimum $E(V,c/a)$ via a polynomial fit to the data points. Note that $c/a$ also varies substantially with temperature,[53] however, as a proof of principles we here only followed its evolution with expanding unit-cell volume. The results are shown in Fig. 14. No dramatic effect results in the global energetics, however the respective

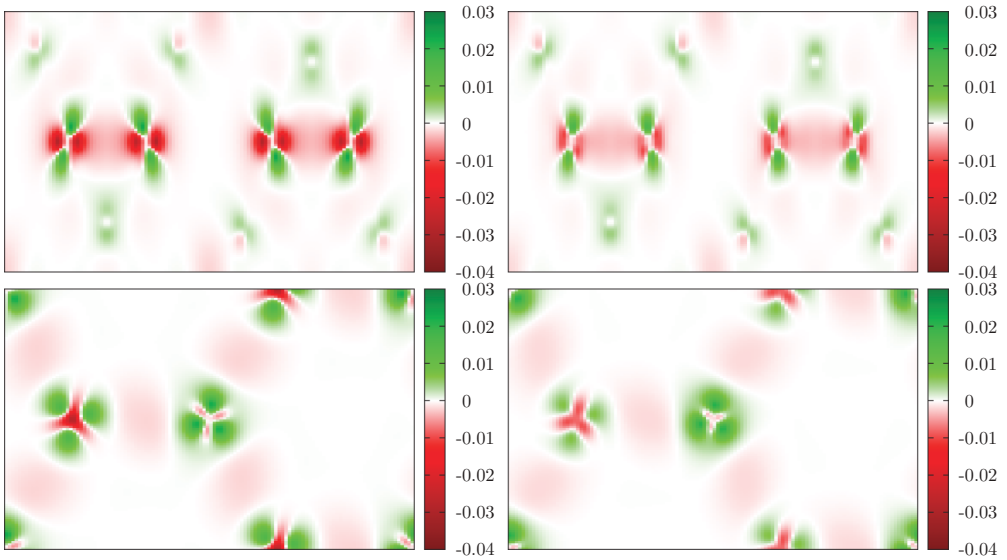


FIG. 11. (Color online) Differences of the electronic charge densities $\rho_{\mathrm{DMFT}}(\underline{r}) - \rho_{\mathrm{LDA}}(\underline{r})$ at $T = 387$ K for the metal with $a = a_0$ (left) and the insulator with $a = 1.1a_0$ (right) within the $xz$ plane (top) and the $xy$ plane (bottom).

energy gain, especially in the PMI phase, is clearly visible. While in experiment the $c/a$ value varies within the interval [2.78,2.88],[52] the given range [2.70,2.80] is somewhat larger from the calculations but still within the right ballpark. In accordance with the experimental data, the PMM phase has a larger $c/a$ than the PMI phase. Interestingly, the minimum ratio is just reached in the transition region with respect to the volume, i.e., $c/a(V)$ becomes most soft close to the negative-pressure-driven MIT. Of course, at the latter first-order transition, a jump in $c/a$ will take place in line with the volume jump corresponding to the tie-line construction.

A relaxation of $c/a$ also affects the trigonal crystal-field splitting $\Delta_{\mathrm{t}}$ between $a_{1g}$ and $e_g'$ orbitals. Because of the lowering of $c/a$ with negative $p$ and hence a weakening of the distortion of the $VO_6$ octahedra, a reduction of $\Delta_{\mathrm{t}}$ is expected. Indeed, the calculations reveal a shrinking of $\Delta_t$ from the PMM to the PMI phase. Note that thereby $\Delta_{\mathrm{t}}$ is determined from the sole Hamiltonian part of the interacting problem stemming from the local-orbital projections acting on the LDA + DMFT converged Bloch states. A second contribution to the resulting *effective* crystal-field splitting $\Delta_{\mathrm{eff}}$ is given by the real part of the self-energy difference between $a_{1g}$ and $e_g'$ at zero frequency, i.e., $\Delta_{\mathrm{eff}} = \Delta_{\mathrm{t}} + \mathrm{Re}\Sigma_{a_{1g}}(0) - \mathrm{Re}\Sigma_{e_g'}(0)$.[44] However, the latter difference differs only little between PMM and PMI and thus no dramatic changes in the occupations occur.

Contrary to that, former post-processing LDA + DMFT studies with an interaction-driven picturing of the difference between PMM and PMI phase resulted in rather strong orbital-polarized solutions for the insulating case. That went along with an enhanced value for $\Delta_{\mathrm{eff}}$ due to large self-energy effects. Note that in the charge-self-consistent LDA + DMFT framework, a clear-cut separation into one- and many-body contributions to $\Delta_{\mathrm{eff}}$ is not that simple anymore. The reason is that during the self-consistency cycle the hoppings also change because of the self-energy effects, contrary to post-processing LDA + DMFT. In our work, we did not change the interaction parameters within the different phases, in line with recent experimental work.[50] We, however, tried to change our global $(U, J)$ parameters in a certain range to look for the possibility of orbital-polarized solutions. Because of the complexity of the problem depending on the interplay of hopping and many-body effects within an evoluting crystal-structure evolution temperature and pressure, we may not exclude a certain setup that allows for orbitally polarized solutions. Yet, within our studies we did not find clear evidence for this behavior.

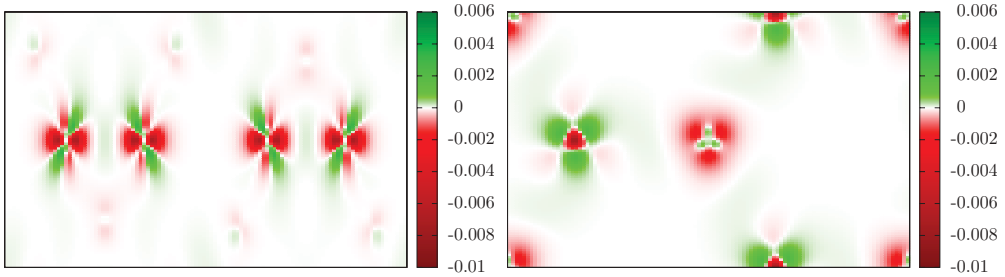


FIG. 12. (Color online) Difference $\rho^{\mathrm{met}}_{\mathrm{DMFT}}(\underline{r}) - \rho^{\mathrm{ins}}_{\mathrm{DMFT}}(\underline{r})$ between the LDA + DMFT charge densities in the metallic ($T = 232$ K) and in the insulating ($T = 387$ K) regime for $a = 1.08a_0$ within the $xz$ plane (left) and the $xy$ plane (right).

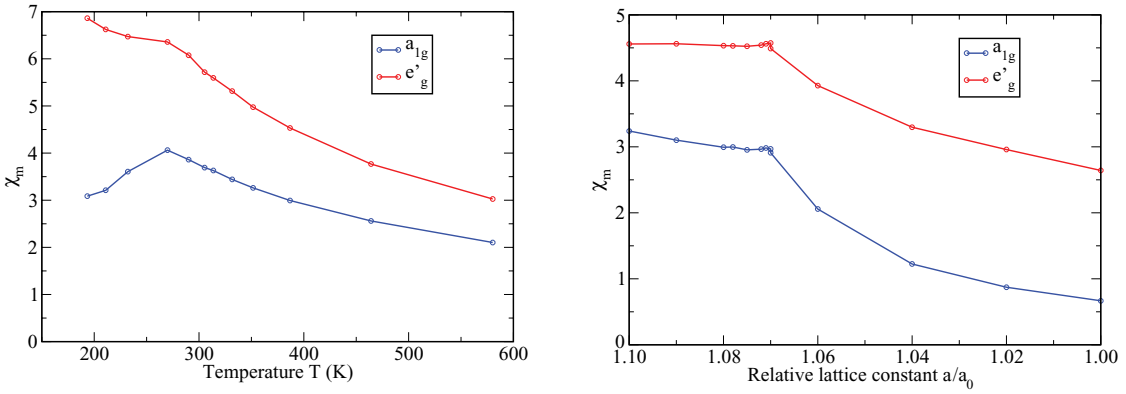


FIG. 13. (Color online) Orbital-resolved local spin susceptibilities with temperature (left) and negative pressure (right).

## IV. SUMMARY AND DISCUSSION

In this work, the advancement of the LDA + DMFT methodology, namely, the implementation of a complete charge-self-consistent scheme with total-energy calculation, built on a pseudopotential band-structure code using plane waves and localized functions, was documented and the principal formalism of interfacing LDA and DMFT utilizing projected local orbitals was reviewed. In the calculations we observed that the charge-self-consistent framework, at least when using a minimal energy window for the projected local orbitals, leads for fixed values of the Hubbard $U$ to somewhat smaller electronic correlations than the elder post-processing scheme. Also, orbital polarizations are generally slightly weaker in the new complete methodology. This outcome might be not that surprising since the now possible reaction of the charge density to the self-energy effects may lead to additional screening effects. Further, more detailed investigations of the charge-self-consistent technique are needed in this respect and shall be hereby stimulated.

As a proof of principles, this approach renders it possible to describe the first-order character of the MIT in the challenging $V_2O_3$ system induced by negative pressure and temperature in accordance with the experimental phase diagram. The methodology is in the position to describe the PMM/PMI phase boundary in a qualitative correct manner. Yet, the quantitative agreement concerning structural data and pressure in the transition region is still not perfect. The neglect of electronic and vibrational entropy terms may be a probable cause, also since the absolute value of the critical negative pressure $|p| < 1$ GPa is rather small compared to other pressure-driven MITs.[54] With increasing lattice constant and elevated temperature, the localization of the electrons is usually energetically favorable because of bond stretching and reduced coherency. But it is known that, e.g., the significant spin-entropy contribution to the true free energy in the PMI phase due to existing localized moments is usually a strong stabilization criterion for the Mott insulator (if that entropy is not quenched by magnetic-ordering tendencies). Including electronic entropy in DMFT is possible, for example, via specific-heat integration or Wang-Landau reweighting techniques.[55] The inclusion of vibrational entropy is more demanding since it asks for a determination of the phonon spectrum, possibly varying with changing static lattice degrees of freedom, and eventually the electronic feedback through electron-phonon coupling.

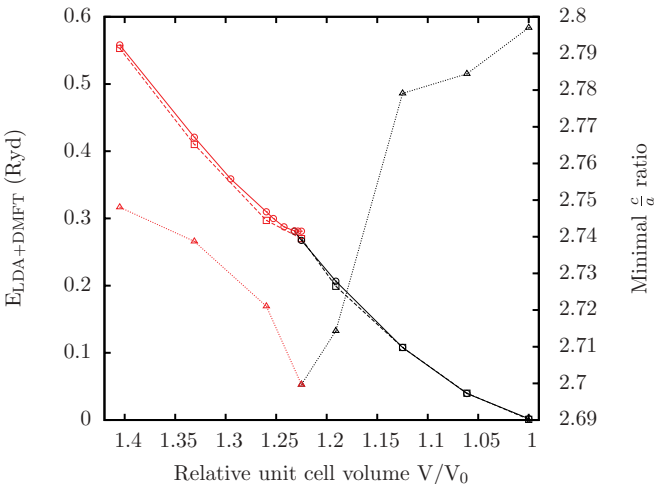


FIG. 14. (Color online) Left panel: Total energy vs volume for fixed $c/a$ (solid line) and relaxed $c/a$ (dashed line). Right panel: Relaxed $c/a$ values vs volume (dotted). Black lines mark the metallic solution, red (gray) lines the insulating one. All data for $T = 387$ K.

At first sight, a qualitative difference concerns the respective orbital ($a_{1g}$, $e'_g$) fillings in the PMM and PMI phases. Whereas polarized x-ray absorption measurements together with multiplet calculations point to an increased orbital polarization towards less filled $a_{1g}$ in the insulating regime,[56] our calculations result in a tendency towards slight orbital balancing in the PMI phase. The named stronger orbital polarization in the insulating regime is indeed verified in post-processing LDA + DMFT for fixed lattice structure, larger $U$, and constant $T$.[43,44] It results there from the increased effective crystal-field splitting due to the strong electronic correlations. However, it is important to note that in the experimental part of the work by Park *et al.*,[56] the negative-pressure regime was realized by nonisovalent Cr substitution for V. Albeit in the latter work no net change in the V valency was detected, since each Cr introduces an additional electron to the system, modifications in the orbital charge distributions may still occur. Rodolakis *et al.*[51,52] compared recently that Cr doping-driven (and thus implicitly negative-pressure driven) MIT with a true pressure-driven MIT. The latter scenario was realized by increasing pressure on insulating $(V_{0.92}Cr_{0.28})_2O_3$. It was observed that with true applied pressure, the orbital

occupations hardly vary at the MIT, in good accordance with our results. Hence, rather strong orbital polarization in the PMI phase appears to be bound to the doping-driven realization of the insulator. Recent ARPES microscopy by Lupi *et al.*[57] of the doped compound suggests that the insulating phase indeed originates from nucleation centers, possibly Cr ions or other defects, as expected for the first-order scenario. Hence, there is a clear need for further theoretical studies that explicitly treat the chemical doping or intrinsic defects. Supercell approaches may be a way to address these issues. The former post-processing LDA + DMFT treatments followed the route of mainly an interaction-driven MIT, while from recent hard x-ray photoemission spectroscopy it was concluded that the Hubbard $U$ does not change through the MIT.[50]

Of course, when it comes to the question of orbital polarization, the competition between crystal-field effects and Coulomb correlations depends on the choice of the interaction parameters $(U, J)$ (Ref. 58) and on the energy window used for the projection onto the correlated subspace. Especially concerning the latter, e.g., inclusion of the O($2p$)-dominated bands (and/or extending the many-body part to a five-orbital sector) will change the notion of the $3d$ orbitals and their overall occupations significantly. More detailed studies along those lines, also by utilizing *ab initio* computed Coulomb integrals, are surely necessary.

Despite this need, this work renders it clear that there is advancement in the LDA + DMFT framework that sharpens the tool for strongly correlated materials investigations of finite-temperature phase competitions on an equal footing with analyses of the involvement of local degrees of freedom.

## ACKNOWLEDGMENTS

We wish to thank L. Boehnke, P. E. Blöchl, I. Leonov, A. I. Lichtenstein, L. Pourovskii, S. Schuwalow, and C. Walther for fruitful discussions. Financial support by the DFG-FOR 1346 is gratefully acknowledged. Computations have been performed at the Regionales Rechenzentrum (RRZ) of the Universität Hamburg as well as the Juropa Cluster of the Jülich Supercomputing Centre (JSC) under Project No. hhh08.

## APPENDIX: REPRESENTATION OF CHARGE DENSITIES IN THE KOHN-SHAM BASIS SETS

In this appendix, we summarize how to compute the given charge density from the matrix $\underline{\underline{\Delta N^{(\underline{k})}}}$ [as in Eq. (12)] in two possible Kohn-Sham basis sets.

### 1. Mixed-basis pseudopotential (MBPP)

The mixed-basis pseudopotential (MBPP) approach[24,59] uses norm-conserving pseudopotentials[60] and a combined basis of plane waves and modified localized atomic functions $\phi^{\underline{k}}_{\alpha lm}(\underline{r})$ for the representation of the crystal wave functions, written as

$$\Psi_{\underline{k}\nu}(\underline{r}) = \frac{1}{\sqrt{\Omega_{\mathrm{C}}}} \sum_{\underline{G}} \Psi^{\underline{k}\nu}_{\underline{G}} e^{i(\underline{k}+\underline{G})\underline{r}} + \sum_{\alpha lm} \beta^{\underline{k}\nu}_{\alpha lm} \phi^{\underline{k}}_{\alpha lm}(\underline{r}), \tag{A1}$$

where $\Psi_{\underline{G}}$ and $\beta_{\alpha lm}$ are the respective expansion coefficients for atom $\alpha$ in the unit cell and angular-momentum numbers $lm$. The correlated charge density therefore consists of three parts $\rho(\underline{r}) = \rho^{(1)}(\underline{r}) + \rho^{(2)}(\underline{r}) + \rho^{(3)}(\underline{r})$, corresponding to a plane-wave term, a mixed term, and a localized-function term. With the abbreviation

$$N^{(\underline{k})}_{\nu\nu'} := f(\tilde{\epsilon}_{\underline{k}\nu})\delta_{\nu\nu'} + \Delta N^{(\underline{k})}_{\nu\nu'}, \tag{A2}$$

they can be written as follows:

$$\rho^{(1)}(\underline{r}) = \frac{1}{\Omega_{\mathrm{C}}} \sum_{\underline{k}\nu\nu'} N^{(\underline{k})}_{\nu\nu'} \sum_{\underline{G}\underline{G}'} \left(\Psi^{\underline{k}\nu'}_{\underline{G}}\right)^* \Psi^{\underline{k}\nu}_{\underline{G}'} \mathrm{e}^{i(\underline{G}'-\underline{G})\underline{r}}, \tag{A3}$$

$$\rho^{(2)}(\underline{r}) = \frac{2}{\sqrt{\Omega_{\mathrm{C}}}} \sum_{\underline{k}\nu\nu'} \mathrm{Re}\left[ N^{(\underline{k})}_{\nu\nu'} \sum_{\underline{G}} \Psi^{\underline{k}\nu}_{\underline{G}} \mathrm{e}^{i(\underline{k}+\underline{G})\underline{r}} \times \sum_{\alpha lm} \left(\beta^{\underline{k}\nu'}_{\alpha lm}\right)^* \left(\phi^{\underline{k}}_{\alpha lm}(\underline{r})\right)^* \right], \tag{A4}$$

$$\rho^{(3)}(\underline{r}) = \sum_{\underline{k}\nu\nu'} N^{(\underline{k})}_{\nu\nu'} \sum_{\alpha lm} \left(\beta^{\underline{k}\nu'}_{\alpha lm}\right)^* \left(\phi^{\underline{k}}_{\alpha lm}(\underline{r})\right)^* \times \sum_{\alpha' l' m'} \beta^{\underline{k}\nu}_{\alpha' l' m'} \phi^{\underline{k}}_{\alpha' l' m'}(\underline{r}) \,. \tag{A5}$$

The first term can be evaluated directly by Fourier transformation of both wave functions to real space. The second and third terms, which are zero in the interstitial region (where the localized functions have decayed), are calculated in a straightforward way in an atom-centered basis.

### 2. Projector-augmented wave (PAW)

The implementation within the PAW formalism is in line with Ref. 17. As shown in Ref. 61, charge densities here break down also into three parts, namely, a plane-wave part $\tilde{\rho}(\underline{r})$ and a one-center term from partial waves $\rho^1_{\underline{R}}(\underline{r})$ and from pseudo-partial waves $\tilde{\rho}^1_{\underline{R}}(\underline{r})$ per atom at site $\underline{R}$ (omitting core densities, which are not affected by our LDA + DMFT approach):

$$\rho(\underline{r}) = \tilde{\rho}(\underline{r}) + \sum_{\underline{R}} \left(\rho^1_{\underline{R}}(\underline{r}) - \tilde{\rho}^1_{\underline{R}}(\underline{r})\right). \tag{A6}$$

The plane-wave part $\tilde{\rho}(\underline{r})$ can be calculated directly as in Eq. (12) from the PAW pseudo-wave functions $|\tilde{\Psi}_{\underline{k}\nu}\rangle$. For the one-center terms, the following one-center density matrix may be defined via

$$\mathcal{D}_{ij} = \sum_{\underline{k}\nu\nu'} \langle \tilde{p}_i | \tilde{\Psi}_{\underline{k}\nu} \rangle \left( f(\tilde{\epsilon}_{\underline{k}\nu})\delta_{\nu\nu'} + \Delta N^{(\underline{k})}_{\nu\nu'} \right) \langle \tilde{\Psi}_{\underline{k}\nu'} | \tilde{p}_j \rangle. \tag{A7}$$

Here, $|\tilde{p}_i\rangle$ are the projector functions from the PAW formalism. With this definition, $\rho^1_{\underline{R}}(\underline{r})$ and $\tilde{\rho}^1_{\underline{R}}(\underline{r})$ can be calculated as usual from the partial waves $\phi_i(\underline{r})$ and from the pseudo-partial waves $\tilde{\phi}_i(\underline{r})$, i.e.,

$$\rho^1_{\underline{R}}(\underline{r}) = \sum_{i,j\in\underline{R}} \mathcal{D}_{ij} \phi^*_j(\underline{r}) \phi_i(\underline{r}), \tag{A8}$$

$$\tilde{\rho}^1_{\underline{R}}(\underline{r}) = \sum_{i,j\in\underline{R}} \mathcal{D}_{ij} \tilde{\phi}^*_j(\underline{r}) \tilde{\phi}_i(\underline{r}). \tag{A9}$$

### 3. Comparison of the present charge-self-consistent scheme to standard LDA + $U$ implementations

In many implementations of the LDA + $U$ scheme, originally designed for long-range-ordered strongly correlated insulators, the local problem is constructed by projecting onto a set of angular-momentum channels (i.e., spherical or cubic harmonics) within a given range around the correlated site. For instance, the LDA + $U$ implementation in the MBPP code as well as in the Vienna *ab initio* simulation package[62,63] (VASP) is performed in such a way. Here, we want to show that the *overall interfacing structure* of the present charge-self-consistent scheme of extending LDA gives similar results as the traditional LDA + $U$ scheme, if a simple purely static mean-field approximation to the local interacting problem is used.

As a simple test, one can compare the variation of the total energy resulting from a conventional LDA + $U$ calculation with the results obtained from the present LDA + DMFT charge-self-consistent calculation now using the Hartree-Fock (HF) approximation for the DMFT impurity solver.

We have calculated the equation of state for $V_2O_3$ within the two approaches and the comparison is shown in Fig. 15. The LDA + DMFT(HF) (or, simply LDA + HF) calculation is performed using the projected local orbitals as defined in Eq. (1) implemented in the VASP code, while the results for the LDA + $U$ scheme are obtained using the standard VASP implementation.[63] The results are rather similar and most of the differences may be due to the alternative choices for the local projections. Note, however, that especially in the general LDA + DMFT context, the local projections as defined in Eq. (1) are clearly superior (e.g., via the resulting well-defined local Green's function) to the simple angular-momentum-channel projections.

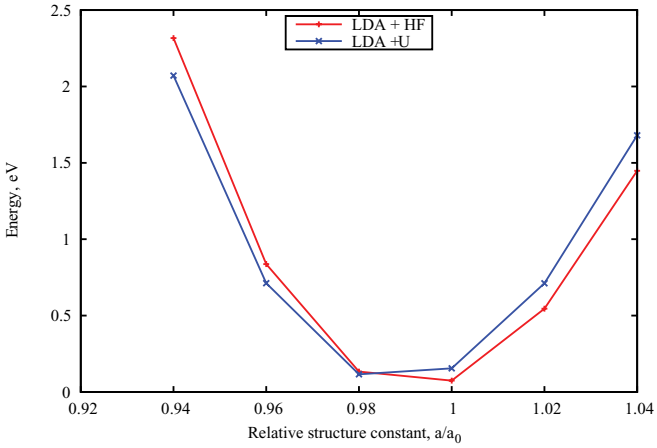


FIG. 15. (Color online) The equation of state of $V_2O_3$ calculated with the conventional LDA + $U$ scheme as well as the charge-self-consistent scheme using a Hartree-Fock solver for the DMFT impurity problem.


[1] N. Saunders and A. P. Miodownik, *CALPHAD: A Comprehensive Guide* (Elsevier, Amsterdam, 1998).
[2] W. Hume-Rothery and H. M. Powell, Z. Kristallogr. **91**, 23 (1935).
[3] W. Hume-Rothery, R. W. Smallman, and C. W. Hawort, *The Structure of Metals and Alloys* (The Institute of Metals, London, 1969).
[4] A. R. Miedema, F. R. de Boer, and P. F. de Chatel, J. Phys. F: Met. Phys. **3**, 1558 (1973).
[5] W. Kohn and L. J. Sham, Phys. Rev. **140**, A1133 (1965).
[6] J. W. D. Connolly and A. R. Williams, Phys. Rev. B **27**, 5169 (1983).
[7] B. L. Gyorffy and G. M. Stocks, Phys. Rev. Lett. **50**, 374 (1983).
[8] S.-H. Wei, A. A. Mbaye, L. G. Ferreira, and A. Zunger, Phys. Rev. B **36**, 4163 (1987).
[9] A. E. Carlsson and J. M. Sanchez, Solid State Commun. **65**, 527 (1988).
[10] S. Müller, J. Phys.: Condens. Matter **15**, R1429 (2003).
[11] F. Lechermann, F. Welsch, C. Elsässer, C. Ederer, M. Fähnle, J. M. Sanchez, and B. Meyer, Phys. Rev. B **65**, 132104 (2002).
[12] G. Kotliar, S. Y. Savrasov, K. Haule, V. S. Oudovenko, O. Parcollet, and C. A. Marianetti, Rev. Mod. Phys. **78**, 865 (2006).
[13] J. Minár, L. Chioncel, A. Perlov, H. Ebert, M. I. Katsnelson, and A. I. Lichtenstein, Phys. Rev. B **72**, 045125 (2005).
[14] L. V. Pourovskii, B. Amadon, S. Biermann, and A. Georges, Phys. Rev. B **76**, 235101 (2007).
[15] K. Haule, C.-H. Yee, and K. Kim, Phys. Rev. B **81**, 195107 (2010).
[16] M. Aichhorn, L. Pourovskii, and A. Georges, Phys. Rev. B **84**, 054529 (2011).
[17] B. Amadon, J. Phys.: Condens. Matter **24**, 075604 (2012).
[18] O. Grånäs, I. Di Marco, P. Thunström, L. Nordström, O. Eriksson, T. Björkman, and J. M. Wills, Computational Materials Science **55**, 295 (2012).
[19] D. B. McWhan, J. B. Remeika, T. M. Rice, W. F. Brinkman, J. P. Maita, and A. Menth, Phys. Rev. Lett. **27**, 941 (1971).
[20] D. B. McWhan, A. Menth, J. B. Remeika, T. M. Rice, and W. F. Brinkman, Phys. Rev. B **7**, 1920 (1973).
[21] S. Y. Savrasov,, K. Haule, and G. Kotliar, Phys. Rev. Lett. **96**, 036404 (2006).
[22] I. Leonov, A. I. Poteryaev, V. I. Anisimov, and D. Vollhardt, Phys. Rev. Lett. **106**, 106405 (2011).
[23] V. Dobrosavljević and G. Kotliar, Phys. Rev. Lett. **78**, 3943 (1997).
[24] B. Meyer, C. Elsässer, F. Lechermann, and M. Fähnle, FORTRAN 90 Program for Mixed-Basis-Pseudopotential Calculations for Crystals, Max-Planck-Institut für Metallforschung, Stuttgart (unpublished).
[25] P. E. Blöchl, Phys. Rev. B **50**, 17953 (1994).
[26] P. Werner, A. Comanac, L. de' Medici, M. Troyer, and A. J. Millis, Phys. Rev. Lett. **97**, 076405 (2006).
[27] M. Ferrero and O. Parcollet, TRIQS: a Toolbox for Research in Interacting Quantum Systems, http://ipht.cea.fr/triqs.
[28] N. D. Mermin, Phys. Rev. **137**, A1441 (1965).
[29] W. Ku, H. Rosner, W. E. Pickett, and R. T. Scalettar, Phys. Rev. Lett. **89**, 167204 (2002).
[30] V. I. Anisimov, D. E. Kondakov, A. V. Kozhevnikov, I. A. Nekrasov, Z. V. Pchelkina, J. W. Allen, S.-K. Mo, H.-D. Kim, P. Metcalf, S. Suga, A. Sekiyama, G. Keller, I. Leonov, X. Ren, and D. Vollhardt, Phys. Rev. B **71**, 125119 (2005).

[31]B. Amadon, F. Lechermann, A. Georges, F. Jollet, T. O. Wehling, and A. I. Lichtenstein, Phys. Rev. B **77**, 205112 (2008).
[32]M. Karolak, T. O. Wehling, F. Lechermann, and A. I. Lichtenstein, J. Phys.: Condens. Matter **23**, 085601 (2011).
[33]F. Lechermann, A. Georges, A. Poteryaev, S. Biermann, M. Posternak, A. Yamasaki, and O. K. Andersen, Phys. Rev. B **74**, 125120 (2006).
[34]S. Y. Savrasov and G. Kotliar, Phys. Rev. B **69**, 245101 (2004).
[35]V. M. Galitskii and A. B. Migdal, Zh. Éksp. Teor. Fiz. **34**, 139 (1958) [Sov. Phys.–JETP **139**, 96 (1958)].
[36]L. Boehnke, H. Hafermann, M. Ferrero, F. Lechermann, and O. Parcollet, Phys. Rev. B **84**, 075145 (2011).
[37]C. Castellani, C. R. Natoli, and J. Ranninger, Phys. Rev. B **18**, 4945 (1978).
[38]L. F. Mattheiss, J. Phys.: Condens. Matter **6**, 6477 (1994).
[39]S. Y. Ezhov, V. I. Anisimov, D. I. Khomskii, and G. A. Sawatzky, Phys. Rev. Lett. **83**, 4136 (1999).
[40]I. S. Elfimov, T. Saha-Dasgupta, and M. A. Korotin, Phys. Rev. B **68**, 113105 (2003).
[41]V. Eyert, U. Schwingenschlögl, and U. Eckern, Europhys. Lett. **70**, 782 (2005).
[42]K. Held, G. Keller, V. Eyert, D. Vollhardt, and V. I. Anisimov, Phys. Rev. Lett. **86**, 5345 (2001).
[43]G. Keller, K. Held, V. Eyert, D. Vollhardt, and V. I. Anisimov, Phys. Rev. B **70**, 205116 (2004).
[44]A. I. Poteryaev, J. M. Tomczak, S. Biermann, A. Georges, A. I. Lichtenstein, A. N. Rubtsov, T. Saha-Dasgupta, and O. K. Andersen, Phys. Rev. B **76**, 085127 (2007).
[45]W. Bao, C. Broholm, S. A. Carter, T. F. Rosenbaum, G. Aeppli, S. F. Trevino, P. Metcalf, J. M. Honig, and J. Spalek, Phys. Rev. Lett. **71**, 766 (1993).
[46]W. Bao, C. Broholm, G. Aeppli, P. Dai, J. M. Honig, and P. Metcalf, Phys. Rev. Lett. **78**, 507 (1997).
[47]O. K. Andersen and T. Saha-Dasgupta, Phys. Rev. B **62**, 16219 (2000).
[48]P. D. Dernier, J. Phys. Chem. Solids **31**, 2569 (1970).
[49]D. B. McWhan, T. M. Rice, and J. B. Remeika, Phys. Rev. Lett. **23**, 1384 (1969).
[50]H. Fujiwara, A. Sekiyama, S.-K. Mo, J. W. Allen, J. Yamaguchi, G. Funabashi, S. Imada, P. Metcalf, A. Higashiya, M. Yabashi, K. Tamasaku, T. Ishikawa, and S. Suga, Phys. Rev. B **84**, 075117 (2011).
[51]F. Rodolakis, P. Hansmann, J.-P. Rueff, A. Toschi, M. W. Haverkort, G. Sangiovanni, A. Tanaka, T. Saha-Dasgupta, O. K. Andersen, K. Held, M. Sikora, I. Alliot, J.-P. Itié, F. Baudelet, P. Wzietek, P. Metcalf, and M. Marsi, Phys. Rev. Lett. **104**, 047401 (2010).
[52]F. Rodolakis, J.-P. Rueff, M. Sikora, I. Alliot, J.-P. Itié, F. Baudelet, S. Ravy, P. Wzietek, P. Hansmann, A. Toschi, M. W. Haverkort, G. Sangiovanni, K. Held, P. Metcalf, and M. Marsi, Phys. Rev. B **84**, 245113 (2011).
[53]L. Baldassarre, A. Perucchi, D. Nicoletti, A. Toschi, G. Sangiovanni, K. Held, M. Capone, M. Ortolani, L. Malavasi, M. Marsi, P. Metcalf, P. Postorino, and S. Lupi, Phys. Rev. B **77**, 113107 (2008).
[54]J. Kunes, A. V. Lukoyanov, V. I. Anisimov, R. T. Scalettar, and W. E. Pickett, Nat. Mater. **7**, 198 (2008).
[55]G. Li, W. Hanke, A. N. Rubtsov, S. Bäse, and M. Potthoff, Phys. Rev. B **80**, 195118 (2009).
[56]J.-H. Park, L. H. Tjeng, A. Tanaka, J. W. Allen, C. T. Chen, P. Metcalf, J. M. Honig, F. M. F. de Groot, and G. A. Sawatzky, Phys. Rev. B **61**, 11506 (2000).
[57]L. B. S. Lupi, B. Mansart, A. Perucchi, A. Barinov, P. Dudin, E. Papalazarou, F. Rodolakis, J.-P. Rueff, S. Ravy, D. Nicoletti, P. Postorino, P. Hansmann, N. Parragh, A. Toschi, T. Saha-Dasgupta, O. K. Andersen, G. Sangiovanni, K. Held, and M. Marsi, Nat. Commun. **1**, 105 (2012).
[58]F. Lechermann, S. Biermann, and A. Georges, Prog. Theor. Phys. Suppl. **160**, 233 (2005).
[59]S. G. Louie, K. M. Ho, and M. L. Cohen, Phys. Rev. B **19**, 1774 (1979).
[60]D. Vanderbilt, Phys. Rev. B **32**, 8412 (1985).
[61]P. E. Blöchl, C. J. Först, and J. Schimpl, Bull. Mater. Sci. **26**, 33 (2003).
[62]G. Kresse and J. Furthmüller, Comput. Mater. Sci. **6**, 15 (1996).
[63]O. Bengone, M. Alouani, P. Blöchl, and J. Hugel, Phys. Rev. B **62**, 16392 (2000).